



Cite this: *Phys. Chem. Chem. Phys.*,  
2024, 26, 3219

# Quantum chemistry and kinetics of hydrogen sulphide oxidation†

M. Monge-Palacios,<sup>†</sup> Q. Wang,<sup>†</sup> A. Alshaarawi,<sup>b</sup> A. C. Cavazos Sepulveda<sup>b</sup>  
and S. M. Sarathy<sup>†</sup>

A fundamental understanding of the acid gas (H<sub>2</sub>S and CO<sub>2</sub>) chemistry is key to efficiently implement the desulphurisation process and even the production of clean fuels such as hydrogen or syngas. In this work, we developed a new kinetic model for the pyrolysis and oxidation of hydrogen sulphide by merging two previously reported models with the goal of covering a wider range of conditions and including the effect of carbon dioxide. The resulting model, which consists of 75 species and 514 reactions, was used to conduct rate of production and sensitivity analysis in plug flow reactor simulations, and the results were used to determine the most prominent reactions in which hydrogen sulphide, molecular hydrogen, and sulphur monoxide are involved. The resulting list of important reactions was screened and the kinetics of three of them, *i.e.*, SO<sub>2</sub> + S<sub>2</sub> → S<sub>2</sub>O + SO, S<sub>2</sub>O + S<sub>2</sub> → S<sub>3</sub> + SO, and SO + SH → S<sub>2</sub> + OH, was found to warrant further investigation. With the goal of improving the accuracy of our new kinetic model, we carried out a robust quantum chemistry and Rice–Ramsperger–Kassel–Marcus master equation study to obtain, for the first time, the forward and reverse rate constants for those three reactions at temperatures and pressures of interest for combustion and atmospheric chemistry. This work is the first step of a kinetic study that is aimed at improving the understanding of the chemistry of the pyrolysis and oxidation of H<sub>2</sub>S, highlighting the importance of sulphur–sulphur interactions and providing a fundamental basis for future kinetic models of H<sub>2</sub>S not only in the field of combustion, but also in atmospheric chemistry.

Received 19th September 2023,  
Accepted 28th December 2023

DOI: 10.1039/d3cp04535h

[rsc.li/pccp](http://rsc.li/pccp)

## Introduction

Raw natural gas (NG) contains levels of hydrogen sulphide (H<sub>2</sub>S) ranging from a few ppm up to 5%.<sup>1</sup> Due to the high toxicity of H<sub>2</sub>S,<sup>2</sup> worldwide health and safety agencies demand the concentration of H<sub>2</sub>S not to exceed 5 ppm in NG before end use.<sup>3</sup> In addition, corrosive H<sub>2</sub>S and other acid gases must be removed from natural gas before pipeline transportation. For the H<sub>2</sub>S removal process, a well-known industrial treatment is the Claus process,<sup>4</sup> in which H<sub>2</sub>S is fully oxidized and converted into solid sulphur and water. Although the main purpose of H<sub>2</sub>S removal is to sweeten NG, H<sub>2</sub>S can also be used to produce clean fuels. For example, partial oxidation of H<sub>2</sub>S may yield hydrogen (H<sub>2</sub>), similarly to methane (CH<sub>4</sub>) combustion under rich conditions.<sup>5</sup> Another feasible treatment is the thermal

decomposition of acid gas, *i.e.*, H<sub>2</sub>S and carbon dioxide (CO<sub>2</sub>), which yields syngas (H<sub>2</sub> and carbon monoxide, CO)<sup>6</sup> that can be used either directly as a fuel<sup>7</sup> or in fuel syntheses (*e.g.*, methanol or Fischer–Tropsch fuels).<sup>8,9</sup> This partial removal of CO<sub>2</sub> in NG is also beneficial since the CO<sub>2</sub> level needs to be below 2% in pipeline-grade methane<sup>1</sup> due to the lack of heating value of CO<sub>2</sub>.

The above-described methods to convert the highly toxic species H<sub>2</sub>S into valuable products can be only optimized and made more efficient by achieving a deep fundamental understanding of the kinetics of the oxidation of acid gas. Therefore, developing an accurate combustion mechanism of H<sub>2</sub>S in the presence of CO<sub>2</sub> is of pivotal importance and is the key to optimize and evaluate the performance of desulphurisation processes and the revalorization of H<sub>2</sub>S, *i.e.*, its conversion into sulphur or the fuels syngas or H<sub>2</sub>.

Nevertheless, both experimental and theoretical works on H<sub>2</sub>S combustion are scarce due to, respectively, the safety issues with H<sub>2</sub>S experimentation and the complexity of the interactions between sulphur species. Binoist *et al.*<sup>10</sup> investigated the pyrolysis of H<sub>2</sub>S in a continuous perfectly mixed quartz tube reactor in the temperature range of 800–1000 °C and proposed a kinetic mechanism with 22 elementary reactions. Zhou *et al.*<sup>11</sup>

<sup>a</sup> King Abdullah University of Science and Technology, Thuwal (Makkah) 23955, Saudi Arabia. E-mail: manuel.mongepalacios@kaust.edu.sa, qi.wang@kaust.edu.sa

<sup>b</sup> Exploration and Petroleum Engineering Center-Advanced Research Center (EXPEC ARC), Saudi Aramco, Dhahran 34465, Saudi Arabia

† Electronic supplementary information (ESI) available. See DOI: <https://doi.org/10.1039/d3cp04535h>

‡ These authors contributed equally.



studied the oxidation of H<sub>2</sub>S in an atmospheric pressure flow reactor from 950 to 1150 K under fuel-lean conditions and developed a kinetic mechanism with 41 species and 277 reactions. The effect of CO<sub>2</sub> on the partial oxidation of H<sub>2</sub>S was investigated by Li *et al.*<sup>12</sup> via tube furnace experiments, who developed a kinetic mechanism with 90 species and 596 reactions. More recently, Stagni *et al.*<sup>13</sup> studied the pyrolysis and oxidation of H<sub>2</sub>S under fuel-lean conditions with jet stirred reactor and flow reactor experiments across a wider range of operating conditions and proposed a kinetic model with 30 species and 156 reactions.

Despite those efforts, discrepancies between experiments and current model predictions remain significant. For example, the discrepancies in the onset of the SO<sub>2</sub> mole fraction profiles, as well as in the peak of the H<sub>2</sub> mole fraction profiles, observed by Stagni *et al.*<sup>13</sup> indicate that reactions in their recent H<sub>2</sub>S combustion mechanism need to be examined further.

At a fundamental level, the interactions between sulphur species under combustion conditions have been rarely studied. Unlike elementary reactions directly related to H<sub>2</sub>S (*e.g.*, hydrogen abstraction from H<sub>2</sub>S by various species), which have been studied by experiments and *ab initio* calculations,<sup>13</sup> reaction pathways and kinetic parameters of most bimolecular reactions involving sulphur-species such as S<sub>2</sub>, SO<sub>2</sub>, S<sub>2</sub>O and SO in kinetic models have been crudely estimated.<sup>11</sup> As an example, the rate constants of 142 out of the 277 reactions in Zhou's model<sup>11</sup> were estimated, and most of these estimated reactions are sulphur-sulphur interactions involving the species S<sub>2</sub>, SO<sub>2</sub>, S<sub>2</sub>O and/or SO. Despite those estimations, this model has been often used as a reference or base model for H<sub>2</sub>S oxidation in later kinetic models, and the same estimations were inherited to even the most up-to-date ones.<sup>12,13</sup> These sulphur species (*e.g.*, SO and S<sub>2</sub>O) represent important intermediates in H<sub>2</sub>S combustion, which are hard to characterize by experiments due to their detection limit. *Ab initio* and kinetic calculations are also complicated due to features such as the multi-reference character, formation of numerous intermediates and saddle points, and pressure effects.

As Raj *et al.*<sup>14</sup> pointed out in a review article, those sulphur-sulphur interactions are extremely important in H<sub>2</sub>S oxidation even under fuel-lean conditions. Therefore, studying the most important reactions of that kind would help to not only improve the performance of current kinetic mechanisms, but also assess the accuracy of the estimations currently being used in these mechanisms.

Under such considerations, this work aims to shed light into the chemistry of H<sub>2</sub>S combustion by first establishing a kinetic model applicable across a wider range of conditions and then by performing quantum chemistry and Rice-Ramsperger-Kassel-Markus master equation (RRKM-ME) calculations<sup>15-17</sup> on some of the most important reactions in the developed model. Therefore, this work highlights the importance of sulphur-sulphur interactions and provides a fundamental basis for future kinetic models of H<sub>2</sub>S oxidation in combustion applications.

Moreover, the chemistry of sulphur species in the atmosphere of the Earth and other planets is limited and thus not

very well understood. Given the low temperature and pressure regimes achieved in our computational kinetic study, the reported rate constants may be also of interest for the development of atmospheric chemistry models that target polluted environments by sulphur emissions<sup>18</sup> or the chemistry of sulphur-containing species in the atmosphere of other planets.

## Computational details and methodology

### Kinetic modelling

Our kinetic model aims to cover a wider range of conditions than former ones and also at including the effect of CO<sub>2</sub> in H<sub>2</sub>S (acid gas) oxidation. Therefore, we merged Li's model for fuel-rich conditions in which the effect of CO<sub>2</sub> was considered<sup>12</sup> and Stagni's model for fuel-lean conditions.<sup>13</sup> Since the latter was developed more recently and included updated rate constants from new *ab initio* calculations and literature, it was used as the base model. When the same reaction was included in both models the corresponding rate constants from Stagni's model were used.

The sub-mechanism for the C/H/O system from Li's model was taken from GRI-3.0,<sup>19</sup> which contains nitrogen chemistry. Since nitrogen chemistry was not anticipated to be relevant in the current H<sub>2</sub>S combustion mechanism, related reactions were removed from the merged model, reducing it by 17 species and 106 reactions. The new H<sub>2</sub>S mechanism contains a total of 75 species and 514 reactions. Fig. 1 shows the corresponding simplified H<sub>2</sub>S reaction path diagram, where it can be seen that in addition to the direct pyrolysis and oxidation products disulphur (S<sub>2</sub>) and sulphur dioxide (SO<sub>2</sub>), intermediates such as sulphur monoxide (SO) and disulphur monoxide (S<sub>2</sub>O) are also important in H<sub>2</sub>S oxidation. Moreover, the reaction path diagram indicates that carbonyl sulphide (COS) is crucial for understanding the effect of CO<sub>2</sub> on H<sub>2</sub>S combustion.

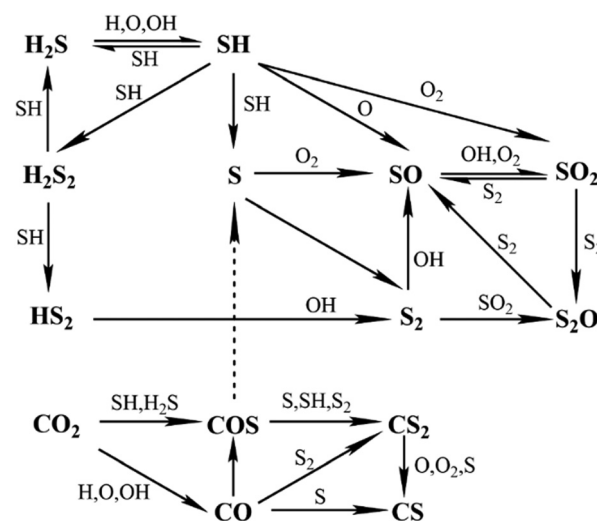


Fig. 1 Simplified reaction path diagram for the H<sub>2</sub>S mechanism developed in this work.



Plug flow reactor (PFR) simulations with CHEMKIN-PRO software<sup>20</sup> using our new model were conducted to get insights into the oxidation of H<sub>2</sub>S. The PFR configuration is the same as Li's experiment setup,<sup>12</sup> namely, with an inner diameter of 16 mm, a length of 800 mm, and an inlet flow rate of 20 cm<sup>3</sup> s<sup>-1</sup>. The simulated conditions are selected as to study the partial oxidation of H<sub>2</sub>S under fuel-rich conditions, in which H<sub>2</sub> and numerous other intermediate species are likely to be formed,<sup>14</sup> *i.e.*, temperatures between 1300 K and 1900 K, fuel composition H<sub>2</sub>S/CO<sub>2</sub>/H<sub>2</sub>O ranging from 18%/81%/1% to 97%/2%/1%, oxidizer composition from air to pure oxygen, and equivalence ratio between 2.0 and 3.0.

Rate of production (ROP) and sensitivity analysis (SA) were performed for the species of interest, namely H<sub>2</sub>S, H<sub>2</sub>, and SO, to identify the most important reactions. H<sub>2</sub>S is the fuel component, thus the ROP and SA were evaluated when its consumption rate is maximized. H<sub>2</sub> is one of the desired products, *i.e.*, a clean fuel, and thus it was analysed when its production rate is maximized. However, since SO is an important partial oxidation intermediate, the corresponding analysis was carried out when its concentration is maximized. The most important reactions were identified and listed at different temperatures, fuel/oxidizer compositions, and equivalence ratios.

It should be noted that the merged kinetic mechanism obtained in this work is being currently validated by means of kinetic modelling and experiments, and it was exclusively used in the current study for the identification of important reactions in the oxidation of H<sub>2</sub>S whose kinetics need to be revisited.

### Quantum chemistry calculations: characterization of the potential energy surfaces

The potential energy surfaces (PESs) of the selected reactions were characterized with the W3X//CCSD/aug-cc-pVDZ, W3X//CCSD/6-311+G(d,p), and W3X//CCSD/jun-cc-pVTZ single point levels of theory, considering their electronic ground-states. Geometries and vibrational frequencies were obtained with the CCSD method<sup>21</sup> and the jun-cc-pVTZ,<sup>22</sup> aug-cc-pVDZ,<sup>22</sup> and 6-311+G(d,p)<sup>23</sup> basis sets depending on the size of the chemical system, and the energy was refined with the composite W3X method.<sup>24</sup> The W3X method incorporates post-CCSD(T) wave function components and complete basis set (CBS) extrapolation schemes in order to estimate highly accurate CCSDT(Q)/CBS energies. Furthermore, thanks to the implementation of the quasi-perturbative quadruple excitations (Q) in the wave function, this method represents a good approach to handle chemical systems with marked multi-reference character or static correlation,<sup>25,26</sup> such as some of those investigated in our work. The optimization and characterization of the stationary points were conducted with the Gaussian16 software<sup>27</sup> and the energy calculations with the W3X method were carried out with the Molpro<sup>28,29</sup> and MRCC software.<sup>30,31</sup>

The minimum energy paths (MEPs) of the investigated reactions were calculated with the Gaussrate17 software<sup>32</sup> by using the Page-McIver method<sup>33</sup> with a mass scaling factor and a stepsize of, respectively, 1.0 amu and 0.02 Å, over the reaction

coordinate range -2.0 to +2.0 Å and evaluating the Hessian matrix every other point. Those MEPs were obtained at the CCSD/jun-cc-pVTZ, CCSD/may-cc-pVTZ or CCSD/6-311+G(d,p) levels of theory depending on the chemical system, and were scaled to reproduce the corresponding W3X single point energy barrier heights for the kinetic calculations. The calculated MEPs were used to confirm the connectivity of the optimized saddle points, reaction intermediates, reactants and products of a given reaction since they were calculated by following the eigenvector of the imaginary frequency and the maximum gradient down from the saddle point. This information is necessary for the RRKM-ME kinetic study, as will be explained in the next Section.

### Rate constant calculations

Using the information of the PES obtained in the previous step for the investigated reactions, we conducted a RRKM-ME kinetic study to calculate the microcanonical flux coefficients and rate constants. The software used for the RRKM-ME calculations was the version 3.1 of TUMME,<sup>34</sup> in which a non-conservative ME with bimolecular pairs was set up and solved to obtain the rate constants of the investigated reactions. The main feature of TUMME is its ability to calculate those microcanonical flux coefficients with the inclusion of torsional and multi-structural anharmonicity, variational, and curvature tunnelling corrections, resulting in accurate rate constants.

First, the high pressure limit rate constants for each of the multiple steps of the selected reactions that have a saddle point were calculated with the Polyrate 2016-2A software<sup>35</sup> using the canonical variational transition state theory (CVT)<sup>36,37</sup> with small curvature tunneling corrections (SCT) and the harmonic oscillator approach (HO),<sup>38</sup> which is defined as

$$k_{\text{SS-HO}}^{\text{CVT/SCT}}(T, s) = \kappa^{\text{SCT}} \frac{1}{\beta h} \frac{Q_{\text{el}}^{\ddagger}(T) Q_{\text{rovib}}^{\ddagger}(T, s)}{\Phi_{\text{el}} Q_{\text{el}}^{\text{R}}(T) Q_{\text{rovib}}^{\text{R}}(T)} \exp(-\beta V_{\text{MEP}}(s)) \quad (1)$$

where  $\kappa^{\text{SCT}}$  is the SCT transmission coefficient,  $\beta$  is  $1/k_{\text{B}}T$ ,  $k_{\text{B}}$  is the Boltzmann's constant,  $T$  and  $s$  are the temperature and reaction coordinate variables, respectively,  $h$  is the Planck's constant,  $V_{\text{MEP}}(s)$  is the classical potential energy of the saddle point defined with respect to that of the reactants,  $\Phi_{\text{el}}$  is the translational partition function per unit volume, and  $Q$  is the partition function with the superscripts  $\ddagger$  and  $\text{R}$  representing transition state and reactants, respectively, and with the subscripts  $\text{el}$  and  $\text{rovib}$  denoting electronic and rovibrational (harmonic), respectively. Furthermore, the low-lying electronically excited state  ${}^2\Pi_{1/2}$  of the OH (140 cm<sup>-1</sup>) and SH (377 cm<sup>-1</sup>) radicals<sup>39</sup> were included in the corresponding reactant and product electronic partition functions to account for the spin-orbit coupling; those partition functions were defined as

$$Q_{\text{e}} = 2 + 2 \cdot \exp(-\varepsilon/k_{\text{B}}T) \quad (2)$$

where  $\varepsilon = 140$  cm<sup>-1</sup> and 377 cm<sup>-1</sup> for the OH and SH reactant and product species, respectively. This effect is assumed to be



fully quenched in the region of the saddle point and reaction intermediates and thus their values for  $Q_e$  is 2.

Second, the density of states of the reaction intermediates and saddle points of those reactions, including torsional anharmonicity, was calculated with the MSTor 2017 software.<sup>40</sup> As for the MSTor calculations, it should be noted that none of those intermediates and saddle points has multiple conformers, and thus multi-structural anharmonicity effects were not implemented in the MSTor calculations.

Finally, the calculated high pressure limit CVT rate constants, together with the corresponding SCT coefficients (CVT/SCT), transition states, and density of states, were provided to TUMME for the RRKM-ME calculations at 0.1, 1.0, 10.0 and 100.0 atm using octuplet precision in the temperature range of 200 K to 3000 K. The bath gas considered for our pressure dependent rate constant calculations was  $N_2$ , and the corresponding Lennard-Jones (LJ) and energy-transfer-down parameters were provided as  $\epsilon = 56.993 \text{ cm}^{-1}$ ,  $\sigma = 3.740 \text{ \AA}$ , and  $\Delta E_d = 200(T/300)^{0.85} \text{ cm}^{-1}$ .<sup>41</sup> Given the limited existing works for sulfur-containing species,  $\Delta E_d$  was selected based on former works for different hydrocarbon and oxygenated reacting species in which  $N_2$  was also used as bath gas.<sup>42–45</sup> For the intermediate species of reactions R1, R2, and R3, which will be defined in the next Section, we used  $\sigma = 4.175 \text{ \AA}$ ,  $\sigma = 4.189 \text{ \AA}$ , and  $\sigma = 3.000 \text{ \AA}$ , respectively, and  $\epsilon = 187.980 \text{ cm}^{-1}$ ; the value of  $\epsilon$  for those intermediates, which is not available in the literature, was derived from the Berthelot combination rule<sup>46</sup> by considering the  $\epsilon$  values of the  $SO_2$  and  $SO_3$  species, *i.e.*, 335.4 K<sup>47</sup> and 218.1 K,<sup>48</sup> respectively.

The rate constants of the barrierless steps of reactions R2 and R3 (see Fig. 4 of the next section) were calculated by providing as input to the master equation the corresponding microcanonical flux coefficients. Those microcanonical flux coefficients were obtained by inverse Laplace transform of the canonical hard-sphere collision flux coefficient, which is calculated as follows for the case of formation of an intermediate INT from a pair of reactants R

$$\hat{k}_{R \rightarrow \text{INT}}(\beta) = \frac{\pi d_R^2}{4} \sqrt{\frac{8}{\pi m_R \beta}} \quad (3)$$

where  $\beta = k_B T$ ,  $m_R$  is the relative-translational reduced mass and  $d_R$  is the effective collision diameter of R. The corresponding reverse rate constants, that is, the dissociation of the intermediate INT into the reactants R, were calculated by detailed balance. This approach to calculate the rate constants of the  $k_{R \rightarrow \text{INT}}$  and  $k_{\text{INT} \rightarrow R}$  association and dissociation reactions may pose a source of error in our final rate constants as the most accurate approach to handle this kind of reactions is the more computationally expensive variable reaction coordinate (VRC) formulation of the transition state theory<sup>49,50</sup> with the right level of theory that can handle the multi-reference character of the transition states.

## Results and discussion

### Rate of production and sensitivity analysis

Rate of production and sensitivity analysis were performed for  $H_2S$ ,  $H_2$ , and SO for 81 different combinations of reactor

temperatures and inlet compositions to identify the most important reactions. It was observed that the top few reactions for each species are the same when changing the inlet compositions (fuel/oxidation compositions and equivalence ratios), and that their prominence depends mainly on the reactor temperature. For the sake of clarity, only a few representative cases are shown in the discussion below for the following initial conditions: 1600 K, fuel composition  $H_2S/CO_2/H_2O = 58\%/41\%/1\%$ , oxidizer as pure oxygen, and equivalence ratios of 2.0, 2.5, and 3.0.

When the  $H_2S$  consumption rate is maximized, the most important reactions are those of  $H_2S$  reacting with OH, H, O, S, and  $S_2$ . All these reactions have been studied either experimentally or computationally and thus the rate constants are considered as adequate for the new mechanism.<sup>2,13,51,52</sup>

The important reactions directly responsible for  $H_2$  production and consumption are well-studied in the literature as well. Therefore, the sensitivity analysis was conducted to investigate how the  $H_2$  production is affected by other reactions and species, as shown in Fig. 2.

The kinetics of the reactions listed in Fig. 2 have been addressed either experimentally or computationally.<sup>13,52–55</sup> However, it is worth noticing that three out of the top six reactions are related to the species SO. As concluded when the simplified reaction path diagram (Fig. 1) was discussed, SO related reactions play an important role in  $H_2$  production and consumption since SO is a key intermediate in  $H_2S$  partial oxidation under fuel-rich conditions. Therefore, we looked into the ROP results for SO, and the top six reactions when the SO concentration is maximized are shown in Fig. 3.

The kinetics of three of the six reactions highlighted in Fig. 3, *i.e.*, the reactions of SO with  $S$ ,<sup>56</sup> O,<sup>53</sup> and  $O_2$ ,<sup>54</sup> has already been investigated. However, for the  $SO_2 + S_2$ ,  $S_2O + S_2$ , and  $SH + SO$  cases, not only their rate constants were estimated in former models, but also their products, *i.e.*,  $S_2O + SO$ ,  $S_3 + SO$ , and  $S_2 + OH$ , respectively, were assumed.<sup>11</sup> To the best of

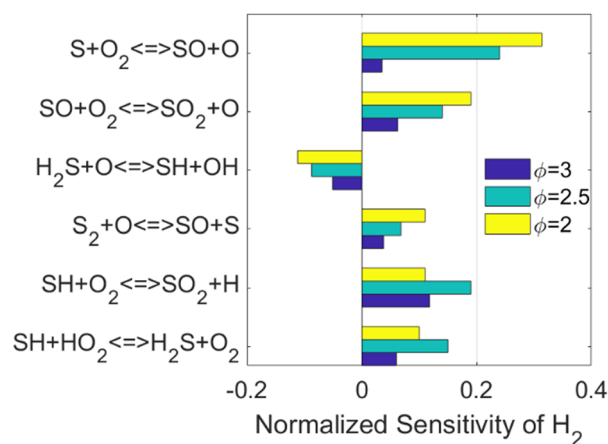


Fig. 2 Normalized sensitivity of  $H_2$  in PFR simulations at  $T = 1600 \text{ K}$ , fuel composition  $H_2S/CO_2/H_2O = 58\%/41\%/1\%$ , and pure oxygen. Yellow, cyan, and blue represent equivalence ratio of 2.0, 2.5, and 3.0, respectively. The reactor coordinates for the maximized  $H_2$  production rate were chosen for the analysis.



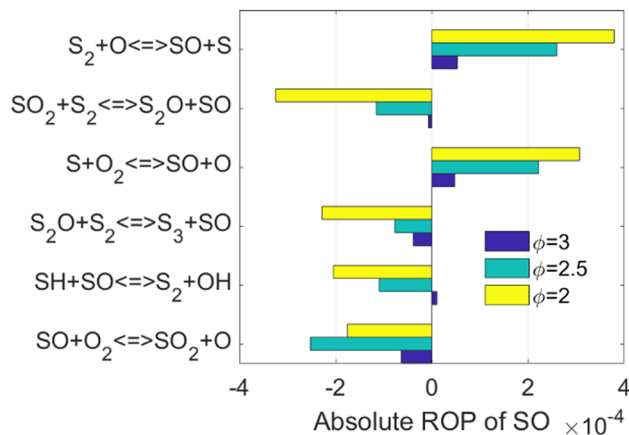


Fig. 3 Absolute ROP of SO in PFR simulations at  $T = 1600$  K, fuel composition  $\text{H}_2\text{S}/\text{CO}_2/\text{H}_2\text{O} = 58\%/41\%/1\%$ , and pure oxygen. Yellow, cyan, and blue represent equivalence ratios of 2.0, 2.5, and 3.0, respectively. The reactor coordinates for the maximized SO concentration was chosen for the analysis.

our knowledge, the kinetics and energetics of the different reaction pathways that those three reactions can go through have not been investigated. Therefore, the reactions  $\text{SO}_2 + \text{S}_2 \rightarrow \text{S}_2\text{O} + \text{SO}$ ,  $\text{S}_2\text{O} + \text{S}_2 \rightarrow \text{S}_3 + \text{SO}$ , and  $\text{SO} + \text{SH} \rightarrow \text{S}_2 + \text{OH}$ , hereafter reactions R1, R2, and R3, respectively, were selected as the target of the current computational kinetic study, which is described in the next Sections.

The rate constants calculated in this work for the selected reactions R1, R2, and R3 will be used to update the newly developed kinetic mechanism.

### Topology of the potential energy surfaces of the target reactions

The reactant pairs  $\text{SO}_2 + \text{S}_2$  and  $\text{S}_2\text{O} + \text{S}_2$  can react on the triplet ground-state and singlet excited-state electronic PESs, yielding ground-state triplet and excited singlet SO, respectively. Similarly, the reactants  $\text{SO} + \text{SH}$  can react either on a doublet ground-state or on a quartet excited state PES, yielding triplet ground-state or singlet excited state  $\text{S}_2$ , respectively. Our computational chemistry study focuses on the more kinetically important electronic ground-states, and the corresponding potential energy profiles of reactions R1, R2 and R3, indicating the connectivity between the different stationary points confirmed by the calculated MEPs, are shown in the panels (a), (b), and (c), respectively, of Fig. 4. Different dissociation channels for the reaction intermediates are displayed by the black and red lines, being those highlighted in red not energetically favoured and thus not kinetically competitive. Therefore, in our RRKM-ME kinetic study, only the pathways represented by black lines were implemented.

The PESs of the three reactions confirm that they take place through a step-wise mechanism with one or more reaction intermediates and saddle points, and thus their rate constants are expected to be not only temperature dependent, but also pressure dependent. With the exception of INT1 of reaction R2, which is an intermediate complex that is probably formed by a

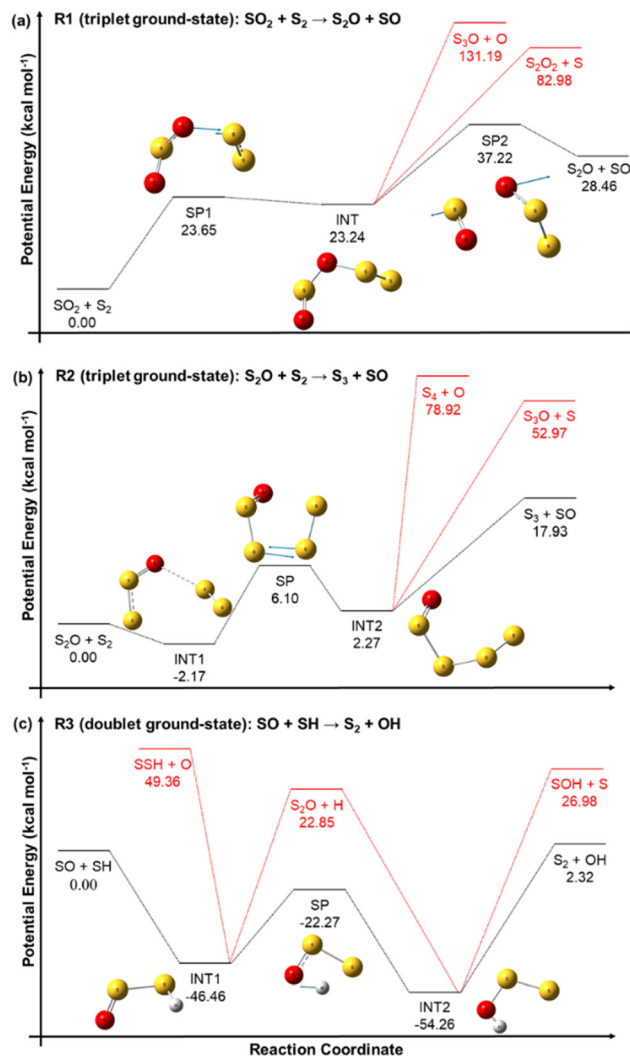


Fig. 4 Electronic ground-state potential energy profiles of reactions R1 (a), R2 (b), and R3 (c) at the  $\text{W3X//CCSD/aug-cc-pVDZ}$ ,  $\text{W3X//CCSD/6-311++G(d,p)}$ , and  $\text{W3X//CCSD/jun-cc-pVTZ}$  levels of theory (black lines), respectively. The eigenvectors of the imaginary frequency of the saddle points are represented by blue arrows, and alternative dissociation pathways of the intermediates are shown with red lines.

dipole-induced dipole weak intermolecular interaction, all the intermediates are covalently bonded species.

The reaction intermediate INT of reaction R1 is more likely to dissociate *via* the S–O bond scission that yields the SO rather than by the S–O bond scission that yields  $\text{S}_3\text{O} + \text{O}$  or the S–S one. Similarly, the reaction intermediate INT2 of reaction R2 is also more prone to dissociate *via* the S–S bond breaking that yields SO. These observations seem to support the importance of the SO species, as discussed before.

The inclusion of the zero point energy corrections in the reaction energies of reactions R1 and R3 to derive the corresponding heat of reactions at 0 K can help with the evaluation of our energy values by comparing them to those derived from the enthalpies of formation tabulated in the Active Thermochemical Tables (ATcT).<sup>57</sup> The heat of reactions  $\Delta H_{\text{R}}(0 \text{ K})$  predicted by our calculations for reactions R1 and R3 are,



respectively,  $28.00 \text{ kcal mol}^{-1}$  and  $3.2 \text{ kcal mol}^{-1}$ , which are in good agreement with the values of  $29.23 \text{ kcal mol}^{-1}$  and  $3.8 \text{ kcal mol}^{-1}$  obtained from the ATcT.

### Rate constants

The forward and reverse rate constants of the step-wise reactions  $R1$ ,  $R2$ , and  $R3$  were calculated with the TUMME software as explained previously in the Rate constant calculations Section. The strongly coupled scheme implemented in MSTor was used for the treatment of torsional anharmonicity of the reaction intermediates and saddle points with more than one torsion, except for the saddle point of reaction  $R2$ , in which both torsional motions were considered as nearly separable.

The calculated forward rate constants of reactions  $R1$ ,  $R2$ , and  $R3$  are represented as a function of temperature in Fig. 5(a), 5(b), and 5(c), respectively, at 0.1, 1.0, 10.0 and 100.0 atm, and the corresponding reverse rate constants are plotted in Fig. 6(a), 6(b), and 6(c). The forward rate constants that Li *et al.*<sup>12</sup> estimated and implemented in their model, which were considered pressure independent, are also plotted for comparison purposes in Fig. 5(a)–(c).

Reaction  $R3$  shows the largest forward rate constants due to its significantly lower endothermicity and barrier height as well

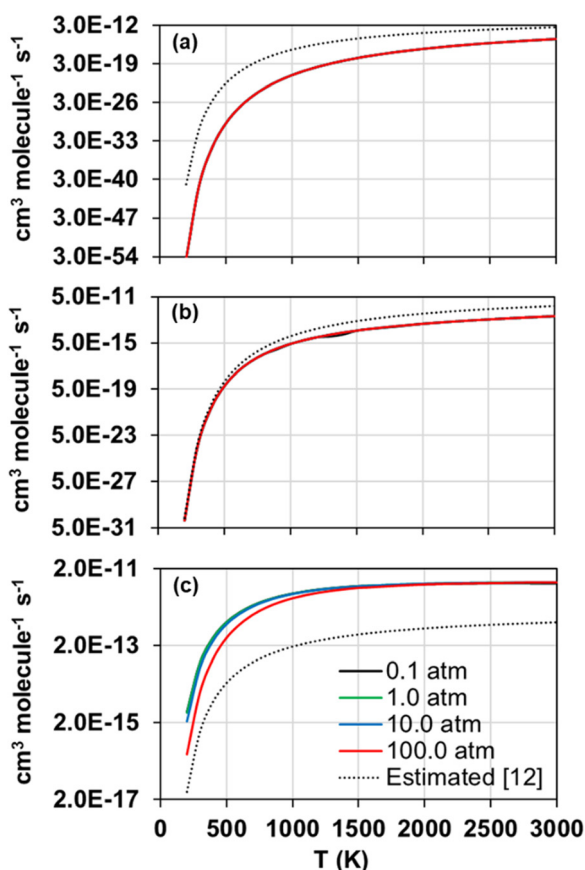


Fig. 5 Calculated (solid lines) forward rate constants of reactions  $R1$  (a),  $R2$  (b), and  $R3$  (c) as a function of temperature at pressures 0.1, 1.0, 10.0 and 100.0 atm. The rate constants estimated by Li *et al.* in their model<sup>12</sup> are also plotted (dotted lines).

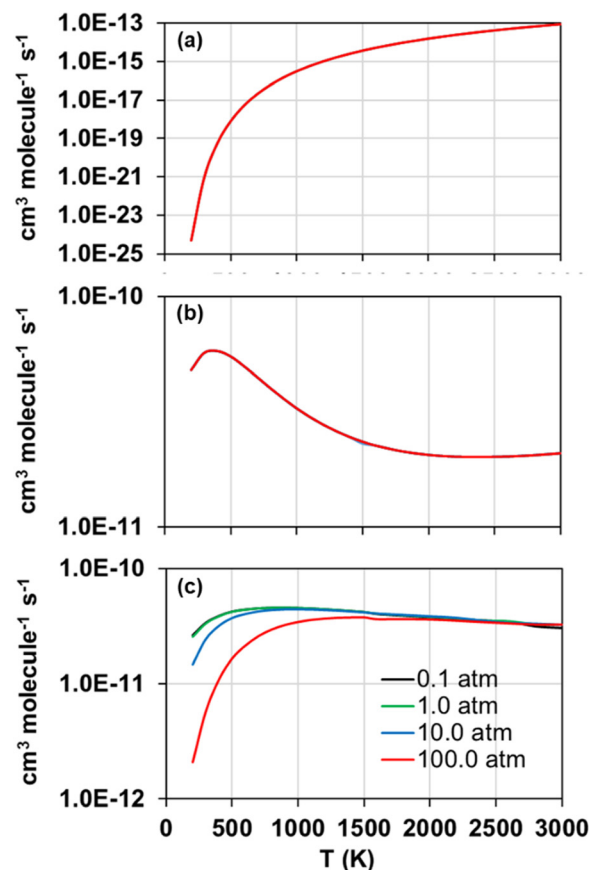


Fig. 6 Calculated reverse rate constants of reactions  $R1$  (a),  $R2$  (b), and  $R3$  (c) as a function of temperature at pressures 0.1, 1.0, 10.0 and 100.0 atm.

as to the significantly larger stability of its reaction intermediates, which make it energetically and kinetically more favoured. On the contrary, reaction  $R1$ , with the largest endothermicity and barrier heights as well as less stabilized reaction intermediates, is the slowest one. Therefore, in the updated model, reaction  $R2$  should control the yield of SO to a larger extent than  $R1$ , especially at lower temperatures when the differences between their rate constants are more pronounced.

The comparison between our calculated forward rate constants and those estimated by Li *et al.*<sup>12</sup> pertain to two aspects. First, the bimolecular products assumed by those authors, which seem to be the correct ones as they are the bimolecular pairs that are most energetically favoured and were confirmed with our MEP calculations as per the connectivity between the different stationary points of the PESs. And second, the value of the rate constants for each reaction, which shows large deviations with respect to our calculations in the case of reactions  $R1$  and  $R3$ , with differences of several orders of magnitude and a severe underestimation in the case of reaction  $R3$ ; on the contrary, the rate constants estimated and calculated for reaction  $R2$  are in much closer agreement, with the largest differences at high temperatures below one order of magnitude. This comparison highlights the need of accurate *ab initio* and kinetic calculations, including pressure dependency, for these and other important reactions whose rate constants were estimated in former kinetic



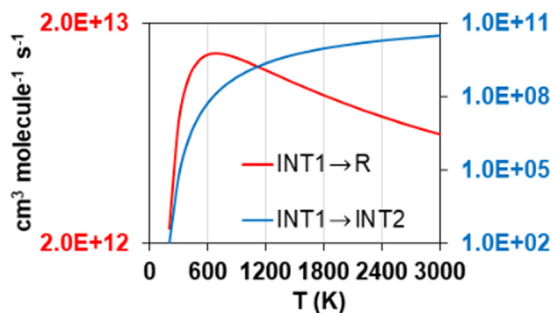


Fig. 7 High pressure limit calculated rate constants of the reactions controlling the flux of the intermediate INT1 of reaction R2 as a function of temperature. Red (left y-axis) and blue (right y-axis) lines correspond to the reactions  $\text{INT1} \rightarrow \text{S}_2\text{O} + \text{S}_2$  (R in the legend stands for reactants, *i.e.*,  $\text{S}_2\text{O} + \text{S}_2$ ) and  $\text{INT1} \rightarrow \text{INT2}$ , respectively.

models in order to improve the accuracy of the future kinetic models addressing the combustion and atmospheric chemistry of  $\text{H}_2\text{S}$ .

As for the reverse rate constants, their temperature dependence shows different trends in the three considered reactions, with an Arrhenius behaviour in the case of reaction R1 but a non-Arrhenius behaviour in the case of reactions R2 and R3; the reverse reaction R1 is the only one with a positive barrier associated to the saddle point SP2, while the other two reverse reactions have submerged barriers that are responsible for the observed non-Arrhenius behaviour, which is usually explained by a change in the sign of the activation energy at a given temperature.<sup>58,59</sup>

Regarding the observed pressure effects in both, forward and reverse reactions, only the rate constants of reaction R3 turned out pressure dependent, showing the typical trend of a chemical activation mechanism involving association intermediates that can be stabilized at high pressures and low

temperatures.<sup>60</sup> Li *et al.*<sup>12</sup> and Zhou *et al.*<sup>11</sup> did not estimate pressure effects not only for any of the three considered reactions in this work, but also for many others whose rate constants were also estimated in their model, suggesting that the kinetics of other reactions may also need to be revisited.

Another distinctive feature of the reverse rate constants of reaction R2 is their positive temperature dependence observed below 400 K, which results in a maximum rate constant value of  $4.78 \cdot 10^{-11} \text{ cm}^3 \text{ molecule}^{-1} \text{ s}^{-1}$  at that temperature. This is attributed to the fate of the intermediate INT1, which is ruled by its decomposition into the reactants  $\text{S}_2\text{O} + \text{S}_2$ , whose rate constants are significantly larger than those of its transformation into INT2. The former, *i.e.*, the step  $\text{INT1} \rightarrow \text{S}_2\text{O} + \text{S}_2$ , shows rate constants with a similar trend to those of the reverse reaction R2, as shown in Fig. 7, where it can be seen that at 700 K they drop to much lower values as temperature decreases. We attribute this change in the rate constants trend of the step  $\text{INT1} \rightarrow \text{S}_2\text{O} + \text{S}_2$ , and thus that in the rate constants of the reverse reaction R2 (Fig. 6(b)), to the fact that the other competing consumption channel of INT1, *i.e.*,  $\text{INT1} \rightarrow \text{INT2}$ , becomes prominent enough at 700 K to also rule the fate of INT1 together with the  $\text{INT1} \rightarrow \text{S}_2\text{O} + \text{S}_2$  channel. In other words, the consumption of INT1 through the  $\text{INT1} \rightarrow \text{INT2}$  channel, which is not kinetically favoured compared to the alternative consumption channel  $\text{INT1} \rightarrow \text{S}_2\text{O} + \text{S}_2$ , hinders the latter channel by lowering its reaction flux only when a high enough temperature is achieved to surmount the barrier associated to the saddle point SP that connects INT1 and INT2.

The values of the different sets of rate constants plotted in Fig. 5 and 6 within the temperature range 200–3000 K are tabulated in Tables 1 and 2, respectively, and they were fitted to the following extended Arrhenius equations ( $A$  in  $\text{cm}^3 \text{ mol}^{-1} \text{ s}^{-1}$ ,  $n$  unitless, and  $E_a$  in  $\text{kcal mol}^{-1}$ ) where  $f$  and  $r$  refer to forward and reverse rate constants, respectively

Table 1 Calculated forward rate constants in  $\text{cm}^3 \text{ molecule}^{-1} \text{ s}^{-1}$  of reactions R1, R2, and R3

$T$ (k)	$k_{R1,f}$	$k_{R2,f}$	$k_{R3,f}^{0.1\text{atm}}$	$k_{R3,f}^{1\text{atm}}$	$k_{R3,f}^{10\text{atm}}$	$k_{R3,f}^{100\text{atm}}$
200	$1.19 \times 10^{-54}$	$2.09 \times 10^{-30}$	$3.84 \times 10^{-15}$	$3.74 \times 10^{-15}$	$2.16 \times 10^{-15}$	$3.07 \times 10^{-16}$
298	$2.53 \times 10^{-41}$	$5.33 \times 10^{-24}$	$7.20 \times 10^{-14}$	$7.10 \times 10^{-14}$	$5.19 \times 10^{-14}$	$1.23 \times 10^{-14}$
400	$3.05 \times 10^{-34}$	$1.10 \times 10^{-20}$	$3.33 \times 10^{-13}$	$3.31 \times 10^{-13}$	$2.74 \times 10^{-13}$	$9.48 \times 10^{-14}$
500	$4.97 \times 10^{-30}$	$8.95 \times 10^{-19}$	$8.23 \times 10^{-13}$	$8.19 \times 10^{-13}$	$7.24 \times 10^{-13}$	$3.25 \times 10^{-13}$
600	$3.55 \times 10^{-27}$	$1.59 \times 10^{-17}$	$1.48 \times 10^{-12}$	$1.48 \times 10^{-12}$	$1.35 \times 10^{-12}$	$7.23 \times 10^{-13}$
700	$4.18 \times 10^{-25}$	$1.20 \times 10^{-16}$	$2.25 \times 10^{-12}$	$2.24 \times 10^{-12}$	$2.11 \times 10^{-12}$	$1.29 \times 10^{-12}$
800	$1.58 \times 10^{-23}$	$5.33 \times 10^{-16}$	$3.04 \times 10^{-12}$	$3.04 \times 10^{-12}$	$2.91 \times 10^{-12}$	$1.98 \times 10^{-12}$
900	$2.76 \times 10^{-22}$	$1.67 \times 10^{-15}$	$3.83 \times 10^{-12}$	$3.82 \times 10^{-12}$	$3.70 \times 10^{-12}$	$2.72 \times 10^{-12}$
1000	$2.82 \times 10^{-21}$	$4.09 \times 10^{-15}$	$4.55 \times 10^{-12}$	$4.55 \times 10^{-12}$	$4.44 \times 10^{-12}$	$3.46 \times 10^{-12}$
1100	$1.94 \times 10^{-20}$	$8.48 \times 10^{-15}$	$5.22 \times 10^{-12}$	$5.22 \times 10^{-12}$	$5.12 \times 10^{-12}$	$4.18 \times 10^{-12}$
1200	$9.84 \times 10^{-20}$	$1.55 \times 10^{-14}$	$5.81 \times 10^{-12}$	$5.81 \times 10^{-12}$	$5.73 \times 10^{-12}$	$4.84 \times 10^{-12}$
1300	$3.96 \times 10^{-19}$	$2.58 \times 10^{-14}$	$6.33 \times 10^{-12}$	$6.33 \times 10^{-12}$	$6.26 \times 10^{-12}$	$5.45 \times 10^{-12}$
1400	$1.33 \times 10^{-18}$	$3.99 \times 10^{-14}$	$6.77 \times 10^{-12}$	$6.77 \times 10^{-12}$	$6.71 \times 10^{-12}$	$5.98 \times 10^{-12}$
1500	$3.84 \times 10^{-18}$	$5.84 \times 10^{-14}$	$7.15 \times 10^{-12}$	$7.15 \times 10^{-12}$	$7.10 \times 10^{-12}$	$6.44 \times 10^{-12}$
1600	$9.81 \times 10^{-18}$	$8.16 \times 10^{-14}$	$7.20 \times 10^{-12}$	$7.33 \times 10^{-12}$	$7.31 \times 10^{-12}$	$6.70 \times 10^{-12}$
1800	$4.81 \times 10^{-17}$	$1.44 \times 10^{-13}$	$7.67 \times 10^{-12}$	$7.84 \times 10^{-12}$	$7.85 \times 10^{-12}$	$7.36 \times 10^{-12}$
2000	$1.76 \times 10^{-16}$	$2.29 \times 10^{-13}$	$8.00 \times 10^{-12}$	$8.23 \times 10^{-12}$	$8.24 \times 10^{-12}$	$7.94 \times 10^{-12}$
2200	$5.21 \times 10^{-16}$	$3.38 \times 10^{-13}$	$8.23 \times 10^{-12}$	$8.51 \times 10^{-12}$	$8.52 \times 10^{-12}$	$8.26 \times 10^{-12}$
2400	$1.31 \times 10^{-15}$	$4.74 \times 10^{-13}$	$8.39 \times 10^{-12}$	$8.70 \times 10^{-12}$	$8.69 \times 10^{-12}$	$8.48 \times 10^{-12}$
2600	$2.89 \times 10^{-15}$	$6.36 \times 10^{-13}$	$8.48 \times 10^{-12}$	$8.85 \times 10^{-12}$	$8.69 \times 10^{-12}$	$8.64 \times 10^{-12}$
2800	$5.78 \times 10^{-15}$	$8.23 \times 10^{-13}$	$8.38 \times 10^{-12}$	$8.78 \times 10^{-12}$	$8.89 \times 10^{-12}$	$8.89 \times 10^{-12}$
3000	$1.06 \times 10^{-14}$	$1.04 \times 10^{-12}$	$8.38 \times 10^{-12}$	$8.94 \times 10^{-12}$	$8.94 \times 10^{-12}$	$8.94 \times 10^{-12}$



Table 2 Calculated reverse rate constants in  $\text{cm}^3 \text{molecule} \times 10^{-11} \text{s}^{-1}$  of reactions R1, R2, and R3

T (K)	$k_{R1,r}$	$k_{R2,r}$	$k_{R3,r}^{0.1\text{atm}}$	$k_{R3,r}^{1\text{atm}}$	$k_{R3,r}^{10\text{atm}}$	$k_{R3,r}^{100\text{atm}}$
200	$4.97 \times 10^{-25}$	$4.78 \times 10^{-11}$	$2.63 \times 10^{-11}$	$2.56 \times 10^{-11}$	$1.48 \times 10^{-11}$	$2.11 \times 10^{-12}$
298	$8.71 \times 10^{-22}$	$5.67 \times 10^{-11}$	$3.38 \times 10^{-11}$	$3.34 \times 10^{-11}$	$2.44 \times 10^{-11}$	$5.76 \times 10^{-12}$
400	$5.82 \times 10^{-20}$	$5.78 \times 10^{-11}$	$3.90 \times 10^{-11}$	$3.87 \times 10^{-11}$	$3.20 \times 10^{-11}$	$1.11 \times 10^{-11}$
500	$7.98 \times 10^{-19}$	$5.47 \times 10^{-11}$	$4.25 \times 10^{-11}$	$4.23 \times 10^{-11}$	$3.74 \times 10^{-11}$	$1.68 \times 10^{-11}$
600	$5.05 \times 10^{-18}$	$4.97 \times 10^{-11}$	$4.43 \times 10^{-11}$	$4.41 \times 10^{-11}$	$4.05 \times 10^{-11}$	$2.16 \times 10^{-11}$
700	$2.02 \times 10^{-17}$	$4.46 \times 10^{-11}$	$4.54 \times 10^{-11}$	$4.53 \times 10^{-11}$	$4.26 \times 10^{-11}$	$2.62 \times 10^{-11}$
800	$6.03 \times 10^{-17}$	$3.99 \times 10^{-11}$	$4.59 \times 10^{-11}$	$4.58 \times 10^{-11}$	$4.38 \times 10^{-11}$	$2.98 \times 10^{-11}$
900	$1.47 \times 10^{-16}$	$3.60 \times 10^{-11}$	$4.59 \times 10^{-11}$	$4.59 \times 10^{-11}$	$4.44 \times 10^{-11}$	$3.26 \times 10^{-11}$
1000	$3.08 \times 10^{-16}$	$3.26 \times 10^{-11}$	$4.56 \times 10^{-11}$	$4.56 \times 10^{-11}$	$4.45 \times 10^{-11}$	$3.46 \times 10^{-11}$
1100	$5.80 \times 10^{-16}$	$2.99 \times 10^{-11}$	$4.51 \times 10^{-11}$	$4.51 \times 10^{-11}$	$4.43 \times 10^{-11}$	$3.61 \times 10^{-11}$
1200	$1.00 \times 10^{-15}$	$2.77 \times 10^{-11}$	$4.45 \times 10^{-11}$	$4.45 \times 10^{-11}$	$4.38 \times 10^{-11}$	$3.71 \times 10^{-11}$
1300	$1.62 \times 10^{-15}$	$2.60 \times 10^{-11}$	$4.38 \times 10^{-11}$	$4.38 \times 10^{-11}$	$4.33 \times 10^{-11}$	$3.77 \times 10^{-11}$
1400	$2.48 \times 10^{-15}$	$2.45 \times 10^{-11}$	$4.29 \times 10^{-11}$	$4.29 \times 10^{-11}$	$4.25 \times 10^{-11}$	$3.79 \times 10^{-11}$
1500	$3.63 \times 10^{-15}$	$2.34 \times 10^{-11}$	$4.21 \times 10^{-11}$	$4.21 \times 10^{-11}$	$4.18 \times 10^{-11}$	$3.80 \times 10^{-11}$
1600	$5.12 \times 10^{-15}$	$2.25 \times 10^{-11}$	$4.04 \times 10^{-11}$	$4.07 \times 10^{-11}$	$4.08 \times 10^{-11}$	$3.66 \times 10^{-11}$
1800	$9.33 \times 10^{-15}$	$2.12 \times 10^{-11}$	$3.90 \times 10^{-11}$	$3.94 \times 10^{-11}$	$3.97 \times 10^{-11}$	$3.67 \times 10^{-11}$
2000	$1.55 \times 10^{-14}$	$2.05 \times 10^{-11}$	$3.77 \times 10^{-11}$	$3.82 \times 10^{-11}$	$3.86 \times 10^{-11}$	$3.64 \times 10^{-11}$
2200	$2.39 \times 10^{-14}$	$2.01 \times 10^{-11}$	$3.66 \times 10^{-11}$	$3.70 \times 10^{-11}$	$3.76 \times 10^{-11}$	$3.55 \times 10^{-11}$
2400	$3.50 \times 10^{-14}$	$2.00 \times 10^{-11}$	$3.55 \times 10^{-11}$	$3.54 \times 10^{-11}$	$3.54 \times 10^{-11}$	$3.45 \times 10^{-11}$
2600	$4.88 \times 10^{-14}$	$2.01 \times 10^{-11}$	$3.45 \times 10^{-11}$	$3.49 \times 10^{-11}$	$3.38 \times 10^{-11}$	$3.36 \times 10^{-11}$
2800	$6.60 \times 10^{-14}$	$2.04 \times 10^{-11}$	$3.14 \times 10^{-11}$	$3.29 \times 10^{-11}$	$3.34 \times 10^{-11}$	$3.29 \times 10^{-11}$
3000	$8.64 \times 10^{-14}$	$2.08 \times 10^{-11}$	$3.04 \times 10^{-11}$	$3.25 \times 10^{-11}$	$3.25 \times 10^{-11}$	$3.28 \times 10^{-11}$

$$k_{R1,f} = 7.94 \times 10^8 \cdot T^{1.074} \cdot e^{(-39000/RT)} \quad (4)$$

$$k_{R2,f} = 1.00 \times 10^{13} \cdot T^{0.029} \cdot e^{(-17956/RT)} \quad (5)$$

$$k_{R3,f}^{0.1\text{atm}} = 2.51 \times 10^{15} \cdot T^{-0.687} \cdot e^{(-4105/RT)} \quad (6)$$

$$k_{R3,f}^{1\text{atm}} = 1.58 \times 10^{15} \cdot T^{-0.624} \cdot e^{(-4064/RT)} \quad (7)$$

$$k_{R3,f}^{10\text{atm}} = 3.16 \times 10^{15} \cdot T^{-0.704} \cdot e^{(-4386/RT)} \quad (8)$$

$$k_{R3,f}^{100\text{atm}} = 7.94 \times 10^{15} \cdot T^{-0.797} \cdot e^{(-5414/RT)} \quad (9)$$

$$k_{R1,r} = 3831 \cdot T^{2.250} \cdot e^{(-9598/RT)} \quad (10)$$

$$k_{R2,r} = 6.31 \times 10^{15} \cdot T^{-0.796} \cdot e^{(-420.3/RT)} \quad (11)$$

$$k_{R2,r}^{0.1\text{atm}} = 1.26 \times 10^{15} \cdot T^{-0.504} \cdot e^{(-723.0/RT)} \quad (12)$$

$$k_{R3,r}^{1\text{atm}} = 1.26 \times 10^{15} \cdot T^{-0.502} \cdot e^{(-742.1/RT)} \quad (13)$$

$$k_{R3,r}^{10\text{atm}} = 1.58 \times 10^{15} \cdot T^{-0.523} \cdot e^{(-980.6/RT)} \quad (14)$$

$$k_{R3,r}^{100\text{atm}} = 2.00 \times 10^{15} \cdot T^{-0.531} \cdot e^{(-1864/RT)} \quad (15)$$

SO when its concentration was maximized. From that rate of production analysis, we concluded that the kinetics of three of the six more important reactions, *i.e.*,  $\text{SO}_2 + \text{S}_2 \rightarrow \text{S}_2\text{O} + \text{SO}$ ,  $\text{S}_2\text{O} + \text{S}_2 \rightarrow \text{S}_3 + \text{SO}$ , and  $\text{SO} + \text{SH} \rightarrow \text{S}_2 + \text{OH}$ , has been just estimated in previous kinetic models due to the lack of kinetic data for sulphur-related reactions.

Therefore, a robust quantum chemistry and Rice-Ramsperger-Kassel-Markus master equation kinetic study have been also conducted in this work for those three reactions, which turned out to proceed through a complex potential energy surface with several intermediates and saddle points. The resulting forward and reverse rate constants, obtained within the wide temperature and pressure ranges of 200–3000 K and 0.1–100 atm, respectively, revealed important pressure effects in the reaction  $\text{SO} + \text{SH} \rightarrow \text{S}_2 + \text{OH}$ , whereas the kinetics of the reactions  $\text{SO}_2 + \text{S}_2 \rightarrow \text{S}_2\text{O} + \text{SO}$  and  $\text{S}_2\text{O} + \text{S}_2 \rightarrow \text{S}_3 + \text{SO}$  is not pressure sensitive. Furthermore, our rate constants calculations also point out large discrepancies with those estimations implemented in former models.

The calculated forward and reverse rate constants for the three selected reactions have been implemented in our new kinetic model with the goal of improving its general performance in the description of the hydrogen sulphide oxidation process, but more specifically, its description of the yield of  $\text{H}_2$  under different conditions as a clean fuel that can be produced from the  $\text{H}_2\text{S}$  carrier.

Moreover, given the low temperatures and pressures considered in our computational kinetic study, we expect our calculated rate constants to also contribute to unravel the chemistry that takes place in polluted environments by sulphur emissions or in the atmosphere of planets that are known to contain sulphur species.

## Author contributions

M. Monge-Palacios and Q. Wang conceptualized the idea of this work, conducted the formal analysis and data curation, and

## Conclusions

A new chemical kinetic model for the oxidation and pyrolysis of  $\text{H}_2\text{S}$  has been developed by merging the previously developed kinetic models by Li *et al.*<sup>12</sup> for fuel-rich conditions, which includes the chemistry of  $\text{CO}_2$ , and that by Stagni *et al.*<sup>13</sup> for fuel-lean conditions. The new model is expected to cover a wider range of conditions than former ones, and was used to carry out plug flow reactor simulations under conditions in which  $\text{H}_2$ , which is targeted as a clean fuel, is more likely to be yielded. From the simplified reaction path diagram of the new model we concluded that the species  $\text{SO}$ ,  $\text{SO}_2$  and  $\text{S}_2\text{O}$  play a pivotal role in the oxidation of  $\text{H}_2\text{S}$ . Moreover, the sensitivity analysis for  $\text{H}_2$  revealed that its production is largely affected by reactions involving  $\text{SO}$ , and thus a rate of production analysis was conducted for





wrote the original draft. M. Monge-Palacios carried out the quantum chemistry and kinetic calculations, and Q. Wang built the updated model and performed the numerical simulations. A. Shaarawi and A. C. Cavazos Sepulveda reviewed the kinetic model, and S. M. Sarathy was responsible for funding acquisition, project administration and supervision, and also reviewed the original draft.

## Conflicts of interest

There are no conflicts to declare.

## Acknowledgements

Research reported in this publication was supported by the Supercomputer Laboratory at King Abdullah University of Science and Technology (KAUST). We would also like to acknowledge the developers of the TUMME software for providing us with the version 3.1 of the software that was used for the kinetics calculations of this work, and specially Dr Rui Ming Zhang for his advice during the setup of the calculations.

## References

- L. Wang and R. T. Yang, *Front. Chem. Sci. Eng.*, 2014, **8**, 8–19.
- T. L. Guidotti, *Int. J. Toxicol.*, 2010, **29**, 551–637.
- M. Rezakazemi, I. Heydari and Z. Zhang, *J. CO<sub>2</sub> Util.*, 2017, **18**, 362–369.
- J. S. Eow, *Environ. Prog.*, 2002, **21**, 143–162.
- Y. Wang, Y. Li, Z. Wang and X. He, *Int. J. Hydrogen Energy*, 2017, **42**, 14301–14311.
- A. M. El-Melih, S. Ibrahim, A. K. Gupta and A. Al Shoaibi, *Appl. Energy*, 2016, **164**, 64–68.
- C. Ghenai, *Adv. Mech. Eng.*, 2010, **2**, 342357.
- X. Cui and S. K. Kær, *Chem. Eng. J.*, 2020, **393**, 124632.
- D. Selvatico, A. Lanzini and M. Santarelli, *Fuel*, 2016, **186**, 544–560.
- M. Binoist, B. Labégorre, F. Monnet, P. D. Clark, N. I. Dowling, M. Huang, D. Archambault, E. Plasari and P.-M. Marquaire, *Ind. Eng. Chem. Res.*, 2003, **42**, 3943–3951.
- C. Zhou, K. Sendt and B. S. Haynes, *Proc. Combust. Inst.*, 2013, **34**, 625–632.
- Y. Li, X. Yu, H. Li, Q. Guo, Z. Dai, G. Yu and F. Wang, *Appl. Energy*, 2017, **190**, 824–834.
- A. Stagni, S. Arunthanayothin, L. Pratali Maffei, O. Herbinet, F. Battin-Leclerc and T. Faravelli, *Chem. Eng. J.*, 2022, **446**, 136723.
- A. Raj, S. Ibrahim and A. Jagannath, *Prog. Energy Combust. Sci.*, 2020, **80**, 100848.
- R. A. Marcus, *J. Chem. Phys.*, 2004, **20**, 359–364.
- H. M. Rosenstock, M. B. Wallenstein, A. L. Wahrhaftig and H. Eyring, *Proc. Natl. Acad. Sci. U. S. A.*, 1952, **38**, 667–678.
- R. A. Marcus, *J. Chem. Phys.*, 2004, **45**, 2630–2638.
- C. N. Hewitt, *Atmos. Environ.*, 2001, **35**, 1155–1170.
- D. M. G. G. P. Smith, M. Frenklach, N. W. Moriarty, B. Eiteneer, M. Goldenberg, C. T. Bowma, R. K. Hnason, S. Song, W. C. Gardiner Jr., V. V. Lissianski and Z. Qin, <https://combustion.berkeley.edu/gri-mech/>.
- CHEMKIN-PRO, Reaction Design, 2019.
- R. J. Bartlett, *J. Phys. Chem.*, 1989, **93**, 1697–1708.
- E. Papajak, J. Zheng, X. Xu, H. R. Leverentz and D. G. Truhlar, *J. Chem. Theory Comput.*, 2011, **7**, 3027–3034.
- K. B. Wiberg, *J. Comput. Chem.*, 1986, **7**, 379.
- B. Chan and L. Radom, *J. Chem. Theory Comput.*, 2013, **9**, 4769–4778.
- M. Monge-Palacios and S. M. Sarathy, *Phys. Chem. Chem. Phys.*, 2018, **20**, 4478–4489.
- J. E. Chavarrio Cañas, M. Monge-Palacios, X. Zhang and S. M. Sarathy, *Combust. Flame*, 2022, **235**, 111708.
- M. J. Frisch, G. W. Trucks, H. B. Schlegel, G. E. Scuseria, M. A. Robb, J. R. Cheeseman, G. Scalmani, V. Barone, G. A. Petersson, H. Nakatsuji, X. Li, M. Caricato, A. V. Marenich, J. Bloino, B. G. Janesko, R. Gomperts, B. Mennucci, H. P. Hratchian, J. V. Ortiz, A. F. Izmaylov, J. L. Sonnenberg, D. Williams-Young, F. Ding, F. Lipparini, F. Egidi, J. Goings, B. Peng, A. Petrone, T. Henderson, D. Ranasinghe, V. G. Zakrzewski, J. Gao, N. Rega, G. Zheng, W. Liang, M. Hada, M. Ehara, K. Toyota, R. Fukuda, J. Hasegawa, M. Ishida, T. Nakajima, Y. Honda, O. Kitao, H. Nakai, T. Vreven, K. Throssell, J. A. Montgomery Jr., J. E. Peralta, F. Ogliaro, M. J. Bearpark, J. J. Heyd, E. N. Brothers, K. N. Kudin, V. N. Staroverov, T. A. Keith, R. Kobayashi, J. Normand, K. Raghavachari, A. P. Rendell, J. C. Burant, S. S. Iyengar, J. Tomasi, M. Cossi, J. M. Millam, M. Klene, C. Adamo, R. Cammi, J. W. Ochterski, R. L. Martin, K. Morokuma, O. Farkas, J. B. Foresman and D. J. Fox, *Gaussian16 software*, 2016.
- H.-J. Werner, P. J. Knowles, G. Knizia, F. R. Manby and M. Schütz, *WIREs Comput. Mol. Biosci.*, 2012, **2**, 242–253.
- H.-J. Werner, *et al.*, MOLPRO, version 2012, a package of ab initio programs, 2012.
- M. Kállay, *et al.*, MRCC, a quantum chemical program suite.
- M. Kállay, P. R. Nagy, D. Mester, Z. Rolik, G. Samu, J. Csontos, J. Csóka, P. B. Szabó, L. Gyevi-Nagy, B. Hégyely, I. Ladjánszki, L. Szegedy, B. Ladóczki, K. Petrov, M. Farkas, P. D. Mezei and Á. Ganyecz, *J. Chem. Phys.*, 2020, **152**, 074107.
- J. Zheng, *et al.*, Gaussrate 17, University of Minnesota, Minneapolis, MN, 2017.
- M. Page and J. W. McIver, Jr., *J. Chem. Phys.*, 1988, **88**, 922–935.
- R. M. Zhang, X. Xu and D. G. Truhlar, *Comput. Phys. Commun.*, 2022, **270**, 108140.
- J. B. J. Zheng, R. Meana-Paneda, S. Zhang, B. Lynch, J. C. Corchado, Y. Chuang, P. Fast, W. Hu, Y. Liu *et al.*, Polyrate 2016-2A software, Minneapolis University of Minnesota, 2016.
- B. C. Garrett and D. G. Truhlar, *J. Chem. Phys.*, 2008, **70**, 1593–1598.
- B. Garrett and D. Truhlar, *J. Phys. Chem.*, 1983, **87**, 4553.
- R. T. Skodje, D. G. Truhlar and B. C. Garrett, *J. Chem. Phys.*, 1982, **77**, 5955–5976.
- M. W. Chase, Jr., J. L. Curnutt, J. R. Downey, Jr., R. A. McDonald, A. N. Syverud and E. A. Valenzuela, *J. Phys. Chem. Ref. Data*, 1982, **11**, 695–940.



- 40 J. Zheng, S. L. Mielke, K. L. Clarkson and D. G. Truhlar, *Comput. Phys. Commun.*, 2012, **183**, 1803–1812.
- 41 B. E. Poling, J. M. Prausnitz and J. P. O'Connell, *Properties of Gases and Liquids*, McGraw-Hill Education, New York, 5th edn, 2001.
- 42 J. P. Senosiain, S. J. Klippenstein and J. A. Miller, *J. Phys. Chem. A*, 2006, **110**, 6960–6970.
- 43 M. Akbar Ali, V. T. Dillstrom, J. Y. W. Lai and A. Violi, *J. Phys. Chem. A*, 2014, **118**, 1067–1076.
- 44 M. Akbar Ali and A. Violi, *J. Org. Chem.*, 2013, **78**, 5898–5908.
- 45 R. M. Zhang, W. Chen, D. G. Truhlar and X. Xu, *Faraday Discuss.*, 2022, **238**, 431–460.
- 46 J. Wisniak, *Educ. Quim.*, 2010, **21**, 155–162.
- 47 J. R. Elliott, V. Diky, T. A. I. V. Knotts and W. V. Wilding, *Properties of Gases and Liquids*, McGraw-Hill Education, New York, 6th edn, 2023.
- 48 X. Tang, P. H. Koenig and R. G. Larson, *J. Phys. Chem. B*, 2014, **118**, 3864–3880.
- 49 Y. Georgievskii and S. J. Klippenstein, *J. Chem. Phys.*, 2003, **118**, 5442–5455.
- 50 Y. Georgievskii and S. J. Klippenstein, *J. Phys. Chem. A*, 2003, **107**, 9776–9781.
- 51 K. Sendt, M. Jazbec and B. S. Haynes, *Proc. Combust. Inst.*, 2002, **29**, 2439–2446.
- 52 C. Wang, G. Zhang, Z. Wang, Q. S. Li and Y. Zhang, *J. Mol. Struct.: THEOCHEM*, 2005, **731**, 187–192.
- 53 C.-W. Lu, Y.-J. Wu, Y.-P. Lee, R. S. Zhu and M. C. Lin, *J. Phys. Chem. A*, 2003, **107**, 11020–11029.
- 54 N. L. Garland, *Chem. Phys. Lett.*, 1998, **290**, 385–390.
- 55 C. Zhou, K. Sendt and B. S. Haynes, *J. Phys. Chem. A*, 2009, **113**, 2975–2981.
- 56 C. Zhou, Kinetic study of the oxidation of hydrogen sulfide, PhD thesis, The University of Sydney, 2009.
- 57 B. Ruscic, R. E. Pinzon, M. L. Morton, G. von Laszewski, S. J. Bittner, S. G. Nijsure, K. A. Amin, M. Minkoff and A. F. Wagner, *J. Phys. Chem. A*, 2004, **108**, 9979–9997.
- 58 S. Y. Mohamed, M. Monge-Palacios, B. R. Giri, F. Khaled, D. Liu, A. Farooq and S. M. Sarathy, *Phys. Chem. Chem. Phys.*, 2022, **24**, 12601–12620.
- 59 M. Monge-Palacios, C. Rangel, J. C. Corchado and J. Espinosa-García, *Int. J. Quantum Chem.*, 2012, **112**, 1887–1903.
- 60 E. Grajales-González, M. Monge-Palacios and S. M. Sarathy, *Combust. Flame*, 2021, **225**, 485–498.

